The interplay between phyllosilicates fabric and mechanical response of deep-seated landslides. The case of El Forn de Canillo landslide (Andorra)

Carolina Seguí, Esperança Tauler, Xavier Planas, Jose Moya & Manolis Veveakis

Landslides
Journal of the International Consortium on Landslides

ISSN 1612-510X
Volume 18
Number 1

Landslides (2021) 18:145-160
DOI 10.1007/s10346-020-01492-6

Springer

Original Paper

Landslides (2021) 18:145–160
DOI 10.1007/s10346-020-01492-6
Received: 22 January 2020
Accepted: 15 July 2020
Published online: 9August 2020

Carolina Seguí · Esperança Tauler · Xavier Planas · Jose Moya · Manolis Veveakis

The interplay between phyllosilicates fabric and mechanical response of deep-seated landslides. The case of El Forn de Canillo landslide (Andorra)

Abstract Deep-seated landslides are among the most devastating natural hazards on earth, usually involving a rigid rock mass sliding over a weak, clayey shear band rich in phyllosilicates. The mechanical response of this shear band to the loading of the overburden is, therefore, critical for the stability and the evolution of a landslide. We hereby show that this mechanical response is strongly associated with mineralogy and microstructure of clay minerals forming the shear band, and vice versa. By presenting a detailed mineralogical, textural, and mechanical characterization of a shear band of an active deep-seated landslide, we attempt to shed light on processes determining the failure mechanism of a large deep-seated landslide. The case study chosen is the El Forn landslide located in Andorra Principality (Eastern Pyrenees). Its shear band is formed of black shales of the Silurian period. Using core samples of this landslide, we have performed mineralogical and microstructural analyses (XRPD, SEM-EDS, and MicroCT), combined with mechanical tests (liquid limit, plastic limit) to study the interplay between the internal texture of the material of the shear band and its mechanical response. Our results show that the highest mechanical alteration of the material occurs at the center of the shear band, where the phyllosilicates are perfectly aligned parallel to the shearing direction. The alignment of the crystals and their face-to-face contact increases the plasticity index of the material and reduces its porosity. Hence, the shearing movement rearranges the contacts of the phyllosilicate grains inside the shear band, reducing the resistance of the material and promoting the slip of the overburden.

Keywords Landslide · Phyllosilicates · Fabric · Shear band · Porosity

Introduction

The shear band of a large deep-seated landslide is the weakest part of the landslide (Kilburn and Petley 2003), admitting chemical and mechanical processes that alter the material and trigger the movement of the sliding mass from its creeping phase to its collapse (Veveakis et al. 2007). Large deep-seated landslides can involve millions of cubic meters of the rock mass, threatening infrastructure and human life in its path, thus creating the need for a deeper knowledge of the processes that occur inside the shear band. Deep-seated landslides can fail because of (1) external factors, changing loading stress of the slope beyond its static limit. Such factors include an increase of groundwater level due to rainfall or artificial dam impoundment, and earthquakes; and (2) internal factors that change the shearing resistance of the shear band material (i.e., strength and friction coefficient) without any variation of the loading stress. Such factors include degradation processes including thermal, hydraulic, and chemical effects (Vardoulakis 2000, 2002; Chang et al. 2005; Veveakis et al. 2007; Goren and Aharonov 2007; Regenauer-Lieb et al. 2009; Goren et al. 2010; Cecinato et al. 2011).

Some of the most prominent effects that could reduce the friction coefficient of the shear band material, for example, are thermal in origin (Anderson 1980; Voight and Faust 1982; Lachenbruch 1980; Mase and Smith 1984; Vardoulakis 2002; Rice 2006). These mechanisms are of primary importance to thermally sensitive materials like clays, making thus very important the knowledge of the material forming the shear band of the landslide and this material's behavior when affected by large deformation and stresses (Vardoulakis 2002). It is very common in large deep-seated landslides to have a shear band formed of clays or clay-like material. This kind of material is challenging with respect to its response under shear, due to its mineralogical composition (i.e., phyllosilicates), especially when these minerals are in contact with water (i.e., groundwater). Saturated clays can become very plastic, which leads to sudden collapses of large deep-seated landslides after years of creeping, as the case of the Vaiont landslide (Italy, 1963) (Veveakis et al. 2007; Segui et al. 2020).

Despite the importance of the microstructure of clay minerals to their macroscopic response, only limited microstructural studies on phyllosilicates (mica group, chlorite group, and clay/clay-like or poorly crystalline phyllosilicates) materials forming landslide shear bands have been performed. The majority of them have been studied for faults located in plate margins (Labaume et al. 1997; Chester and Logan 1987; Collettini et al. 2009), and one for the Walton's Wood landslide (Tchalenko 1968). All of these studies show that inside the shear band phyllosilicates are fully oriented and aligned parallel to shear movement, and outside the shear band, the fabric of clays is randomly oriented. All of them also agreed that the alignment of clay minerals inside the shear band affects the shearing resistance of the material, decreasing its friction coefficient (Labaume et al. 1997; Chester and Logan 1987; Collettini et al. 2009; Tchalenko 1968). Maltman (1987) studied experimentally the microstructure of a clayey shear band and stated that the alignment of phyllosilicates in the shear band is not due to the flow of groundwater but due to an intense shear movement. Labaume et al. (1997) linked the orientation of phyllosilicates inside the shear band with a compactant plastic strain behavior of the clays.

Studies performed regarding possible failure mechanisms of large deep-seated landslides focusing on the shear band behavior include mechanical parameters of the clayey material of the shear band and its response to external factors (such as groundwater variations) (Vardoulakis 2000, 2002a; Veveakis et al. 2007; Goren and Aharonov 2007; DeBlasio and Elverhoi 2008; Goren et al. 2010; Regenauer-Lieb et al. 2009; Chang et al. 2005; Ferri et al. 2011; Cecinato and Zervos 2012; Segui et al. 2020). Moreover, studies that have focused on the current case study—El Forn landslide

(Andorra)—have not included the response of the shear band material and its impact on landslide failure. Firstly, Corominas and Alonso (1984) and Soutadé (1988) presented the landslide and its history, respectively. Corominas (1990) described its slope stability, and Santacana (1994) and Planas et al. (2011) presented the history of movements that occurred in the landslide. More recently, Jaqués (2014) proposed the latest geological model of the landslide with a new history of movements of the slide and an analysis of slope stability. Jaqués (2015) also studied the general and local behavior of the active landslide. Finally, Corominas et al. (2015) followed the sliding movement by radar and differential interferometry techniques.

The present work extends these studies by focusing on the role of microstructural response (fabric) of phyllosilicates in the macroscopic response of deep-seated landslides. We present as a case study the El Forn landslide (Andorra, Eastern Pyrenees), which is the largest active deep-seated landslide in the Pyrenees, involving a mass of approximately 300 Mm^3 (Corominas et al. 2013). In the following sections, we firstly present the case study of El Forn landslide, before detailing the methods used for microstructural and mechanical characterization of landslide's materials. Following this, the results of these studies, in combination with appropriate field data, are presented and thoroughly discussed.

Case study: El Forn de Canillo landslide

El Forn landslide is located on the southern side of the Pyrenees, on the left margin of the Valira d'Orient river basin, near Canillo village (Fig. 1). The landslide is a huge complex earthflow having more than 300 Mm^3 and extending about 2.7 km^2 (Corominas et al. 2013) (Fig. 1c). The landslide is an old one with some parts being presently active, which affects a village, several farms, and a road (Jaqués 2014, 2015) as it is described below, motivating its monitoring and study since the 1980 decade.

The landslide has been formed by several destabilizations since the Upper Pleistocene leading to accumulations of large slide deposits. It was first described by Corominas and Alonso (1984) and after by Soutadé (1988), who postulated that the mass slid towards the valley after the Valira d'Orient glacier melted between 20.000 and 10.000 BP (Before Present). After these initial studies, Corominas (1990) described the influence of the glacier retreat on the stability of El Forn and Encampanada (nearby site) slopes. Santacana (1994) studied in depth the large earthflow of El Forn and the lateral expansion of Encampanada, which resulted from the retreat of the Valira d'Orient glacier in the main valley, between 16.000 and 13.000 BP or lower. The latter author identified three main episodes in the formation of El Forn landslide: The first is a complex rotational/translational movement with the flow at the toe at the western margin of the El Forn area, which could have collapsed the main valley; the second is also a rotational/translational complex movement that dammed the valley, and the third is a rotational movement that buried some areas of the rotational sections of the second movement. Santacana (1994) also pointed out that there are recent movements at the toe of the landslide.

Planas et al. (2011) studied exhaustively the movements produced in the El Forn landslide following the work of Santacana (1994) and using borehole logs, detailed field mapping, and radiocarbon dating. Planas et al. (2011) concluded that El Forn landslide has been subject to at least three main episodes of movement and revealed that the two older occurred within the glacial period and that both involved a (slow) progression of the glacier over the sliding mass. Jaqués (2014, 2015) proposed a new model for the landslide history and used limit equilibrium and finite element methods to analyze the behavior of the entire slide and the most active bodies of the sliding mass.

The active parts of the landslide involve two main risks: (1) the sliding area includes the small village of Prats and several residential areas; (2) the landslide is sliding towards Canillo village (north-west direction). Displacement indicators (as fractures and subsidence in the roads and fissures on walls of buildings and retaining walls) revealed the activity of some sectors of the landslide and motivated the Andorra Government to develop landslide and risk maps (Altimir et al. 2001; Euroconsult 2002). To assess more quantitatively the risk and to construct a system for early warning, the Andorra Government complemented these studies with a surveillance plan. It involved borehole drilling along the entire landslide to monitor the displacements (borehole extensometers and inclinometers) and groundwater levels (piezometers (Euroconsult 2007)). More recently, radar differential interferometry techniques (GB-SAR and DInSAR) were also performed to monitor the displacement in a more distributed way (Corominas et al. 2013, 2015).

Monitoring from 2008 to 2018, three active parts in the landslide were identified: Cal Ponet–Cal Borronet (center-north), Clots Fondos (north-east), and Prats (at the toe of the slide, east) with maximum velocities of approximately 4 cm/year. Figure 1d shows the displacement of Cal Ponet–Cal Borronet lobe between April and June of 2017 with a movement of over 0.5 cm (Euroconsult 2017). Previous studies have suggested that triggering factors of this landslide are (1) rise of groundwater level and (2) erosion at the toe of the landslide due to the Valira d'Orient river (Corominas et al. 2015).

In this study, we will focus on the Cal Ponet–Cal Borronet lobe (Fig. 1c). This lobe has been described and delimited by Torrebadella et al. (2009) as one of the active and fastest creeping lobes of the El Forn landslide involving a mass of 0.97 Mm^3. Torrebadella et al. (2009) presented the results of the group of lithologies present in the landslide from core samples obtained between 2007 and 2009, which are divided by three main groups: colluvium, high fractured and altered shales, and bedrock shales. Furthermore, Torrebadella et al. (2009) showed the results of geotechnical parameters of each group of geological units for each borehole performed and the instrumentation installed inside the boreholes. By the time Torrebadella et al. (2009) concluded the report, with field data to describe the areas of the landslide that were active and creeping faster at that time, the authors defined the Cal Ponet–Cal Borronet lobe.

Focusing now on the Cal Ponet–Cal Borronet lobe, the first borehole was performed in 2007 with core sample recovery—which is the material that has been used in this study—and instrumented with piezometers and inclinometers. Due to the movement of the landslide and, thus, the loss of some instrumentation of the borehole below the shear band (due to continuous displacement of the mass), the Andorra Government has performed 4 additional boreholes next to the initial one to continue monitoring its movement and groundwater. The last borehole and installation of the instrumentation were carried out by the Andorra Government and the Polytechnic University of

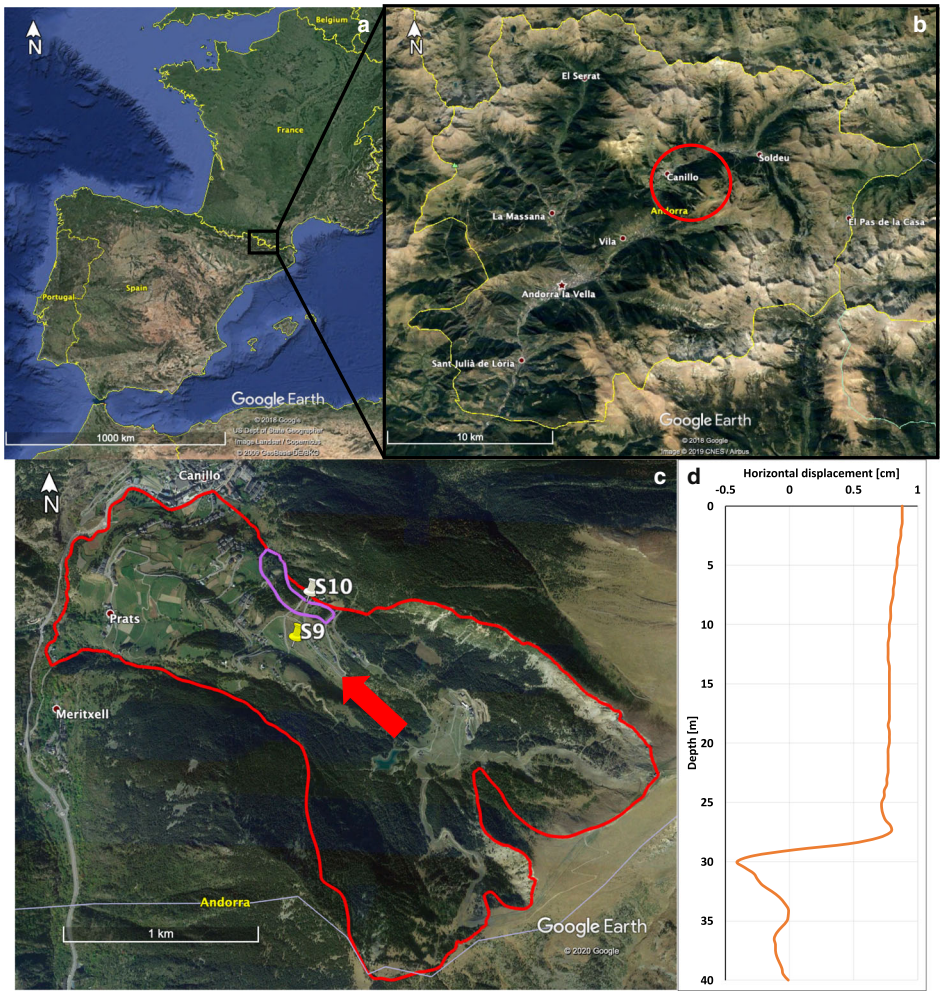

Fig. 1 **a** Satellite image (©Google Earth) of the SW of Europe, where Andorra Principality is located inside the black square. **b** Satellite image (©Google Earth) of Andorra Principality with a red circle indicating the location of the study area (near Canillo). **c** Satellite image (©Google Earth) presenting El Forn landslide (in red), the red arrow indicating the direction of movement of the sliding mass, Cal Ponet–Cal Borronet lobe (in purple) with the location of the S10 borehole (white marker) and the S9 borehole (yellow marker). **d** Displacement data of S10 borehole from April to June 2017 (Euroconsult 2017)

Catalonia (UPC). This last borehole was performed in September of 2018, which did not have core sample recovery; however, it was instrumented with three piezometers at different depths (one below the shear band and two above it), a wire extensometer (Corominas et al. 2000) (with the base at 40 m depth) and a thermometer in the shear band at 29 m depth.

Geological setting

From a geological point of view, Andorra country is located in the central-eastern part of the Pyrenean Axial Zone. Therefore, due to the orogeny of the Pyrenees, the structural morphology of Andorra Principality is complex because it includes anticlines, synclines, and faults (see Hartevelt 1970; Zwart 1979; Barnolas and Chiron 1996) formed of Paleozoic materials (Cambrian, Ordovician Silurian, and Devonian) that have been intensely deformed in a complex process during long periods (Clariana 2004). These geological materials are associated with detachments and diapirs causing softness and incompetent behavior (Zwart 1979).

Geological map (Fig. 2) presents the area of interest in this study, which is the El Forn landslide (defined by a thick black line) that is formed of Paleozoic materials (Cambro-Ordovician to Mid Devonian), and the Cal Ponet–Cal Borronet lobe (defined by a thick red line) formed of Silurian materials. Silurian materials (inside the Paleozoic age) are present as limestone and shale (in green) from the W to SE areas of the landslide. Moreover, there are three formations of the Devonian at the E and NE part of the landslide: (1) marly limestones and vivid color shales of the Lower-Mid Devonian (in light orange), and two intrusive contacts of the lower Devonian as (2) massive limestones (in dark gray) and (3) alternations of limestones and brown shales (in blue). At the SE part of the landslide, there are series of rhythmic sandy shales (in white) of the Cambro-Ordovician (see Clariana 2004 for a detailed stratigraphy).

Geological structures in this region are arranged in E-W or ENE-WSW direction. Pre-carboniferous materials are present as anticline and syncline domes with large extensions (kilometers) with faults and thrusts at the boundaries of these domes oriented in the same direction as the domes. The El Forn landslide area is located at the Tor-Casamanya syncline, where Devonian materials are present at the center of the landslide and Silurian and Cambro-Ordovician materials are located at the sides of the landslide (Clariana 2004).

Methodology

Samples used in the study

The samples preserved of the 2007 borehole of Cal Ponet–Cal Borronet lobe are shown in Fig. 3 (from 25 to 30 m depth), where the shear band is located (at 29 m depth). It is known that these samples are fully saturated due to the information provided by the piezometers (Euroconsult) and Fig. 3. The shear band is located between 28 and 31 m depth as identified by the data provided by extensometers and inclinometers (Euroconsult and UPC). The profile of vertical displacement of the Cal Ponet–Cal Borronet lobe (Fig. 1d) shows that the sliding mass is moving as a rigid block (translational/rotational).

The core samples (Fig. 3) show three main facies. The first facie is from 25 to 26 m depth where samples are large blocks (looks as cohesive material) in white/gray colors. From 26 to 27-m depth samples are incohesive (looks as a weaker material than the above) in a darker color with green tones. Finally, from 27 to 30-m depth samples are also incohesive as 26–27 m depth but darker with black and gray tones. These changes in color indicate the presence of different minerals, which are detailed in the "XRPD" section.

The grain size of the samples from 27 to 30 m depth has been defined by three main sizes: (1) chips from decimeters (dm) to centimeters (cm), (2) flakes from cm to millimeters (mm), and (3) powder size as micrometers (μm). Figure 3 shows that the samples seem homogeneous from outside, with orange stains that indicate a process of oxidation. Inside the samples can be seen quartz veins (white color) that are surrounded by very fined and homogeneous gray shales. The fractures in these samples are most of them totally or partially filled by quartz. Moreover, all the samples present organic matter, which is detected as the samples tinge fingers with black-gray color.

These core samples (Fig. 3) have been divided at each half a meter of depth to perform tests to characterize the shear band. Therefore, we ended up with 9 samples to characterize the geological material and the evolution (in-depth) of its properties. Furthermore, we studied core samples of Silurian shales located at the bedrock (174–175 m depth) and obtained from the S9 borehole (Fig. 1c). The Silurian shales of the bedrock have been studied to compare "pure" shales (bedrock's material) with "altered" shales (shear band's material).

Analytical techniques

X-ray powder diffraction

Samples studied in X-ray powder diffraction (XRPD) needed to be crushed in an agate mortar until the rock reduces its particle size below 40 μm, ending up with a very fine powder that does not scrape between the fingers. XRPD data were collected with Panalytical X'Pert PRO MPD X-ray diffractometer with monochromatized incident Cu Kα1 radiation at 45 kV and 40 mA, equipped with a PS detector with an amplitude of 2.113°. Patterns were obtained by scanning randomly oriented powder particles from 4 to 80° (2θ). Datasets were obtained using a scan time of 50 s at a step size of 0.017° (2θ) and variable automatic divergence slit. The identification of minerals was achieved by comparing XRPD diffractogram with the ICDD database (2007 release) using the Diffrac plus evaluation software (Bruker 2007). Quantitative mineral phase analyses were obtained by full refinement profile using XRPD and the software TOPAS V4.2 (2009) (Coelho 2000).

Scanning electron microscope with energy-dispersive X-ray spectroscopy

To study samples in SEM-EDS, we have created polished thin sections from the core samples. The procedure of the sample preparation of a thin section includes cutting a 1000-mm^3 cubical or prismatic sample from a cylindrical core of undisturbed material retrieved at a depth between 27–30 m (shear band) and 174–175 m (bedrock). A cubical sample is first included in epoxy resin and then attached on a glass sample holder—on one side—to cut a slice of 50 μm thick on which SEM observations will be performed. Finally, a metallographic polishing—under dry conditions—is carried out to obtain the flat surface needed for EDS analyses. Morphology and microtextural features of the studied samples were examined with Nikon Eclipse LV100 POL microscope and ESEM Quanta 200 FEI, XTE 325/D8395 scanning electron microscope with energy-dispersive X-ray spectroscopy (SEM-EDS).

Micro X-ray computed tomography scanner

Micro X-ray computed tomography (MicroCT) tests have been performed on the studied core samples. Multiple tests have been performed to ensure the representativeness of the samples and repeatability of the results. The porosity of the studied samples was examined on chips of original core rock (order of cm) with a Nikon XTH 225 ST, which is a high-resolution X-ray computed tomography scanner. With this scanner, 2D and 3D images inside and outside the sample are obtained by projection of X-ray beam through the sample and sample's interaction with the beam via radiography/X-ray image. The X-ray source used in the tests performed is the 225-kV UltraFocus Reflection Based Signal and Tungsten Target (spot size 3 μm) with a max power of 200 W. The detector used is the Perkin Elmer 1620 AN3 CS CT. The X-ray filter used is a 0.5-mm thick copper filter. We have used the Avizo software (TJP 2015) to post-process the 2D MicroCT images. The 3D reconstruction and the quantification of the matrix and the porosity, separately, have been performed by segmenting the 2D images (i.e., separate the pores from the matrix using a gradient threshold method). Once the segmentation is successful (i.e., the contacts between the matrix and the pores are well defined, as well as the contour of the sample from the background), the quantification of the volumes is automatic by the Avizo software. To quantify the volume of pores and the volume of the matrix, the software uses the voxel size of the image, the 3D reconstruction, and the segmentation.

The technical features of MicroCT scanner images include resolution (voxel size) between 0.0265 and 0.0443 mm, detector

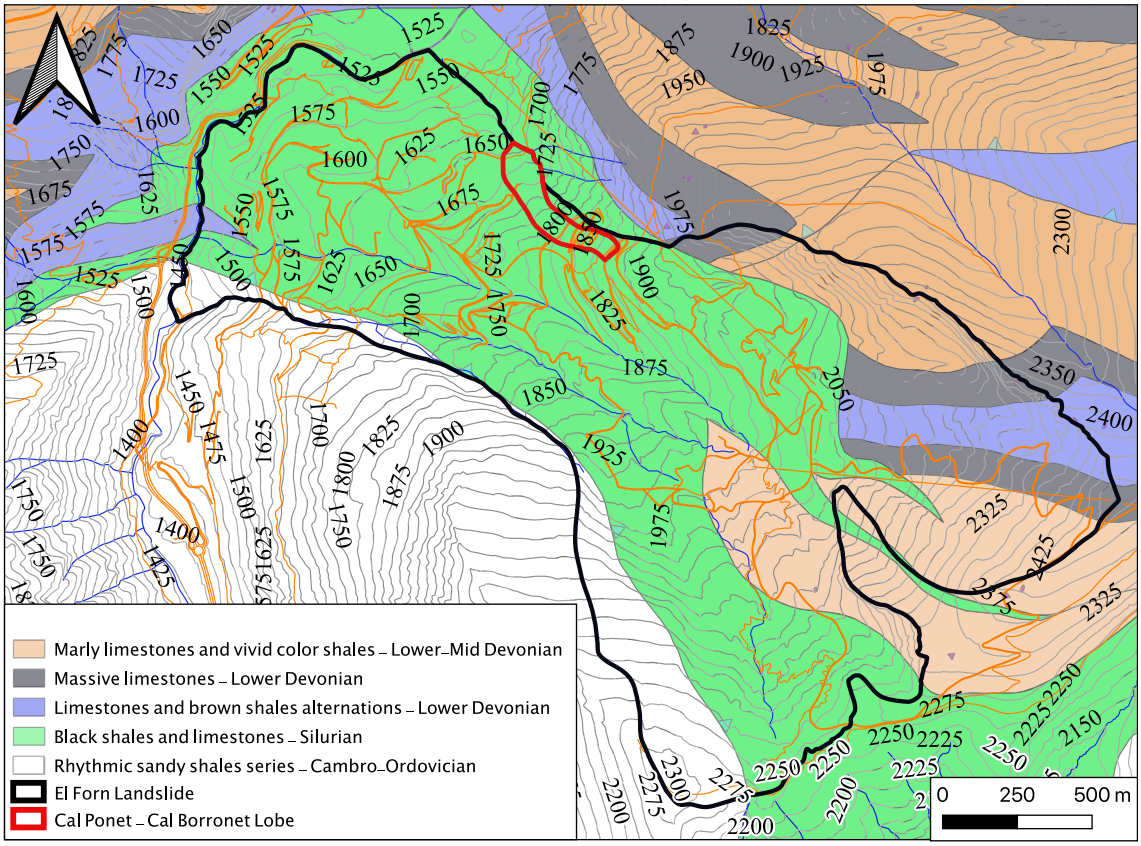

Fig. 2 Geological map of the study area (modified after Clariana 2004)

2000 × 2000 pixels with each pixel spaced at 200 μm, 2500 projections, angle steps of 0.144°, and X-ray energy of 190 kV.

Plasticity index

The plasticity index has been obtained for the studied samples. For each sample, we have performed three tests to obtain reliable results. First, it has performed a plastic limit test, and second a liquid limit test using Casagrande's liquid limit device. Both tests, liquid limit and plastic limit, have been performed following the standard approach in soil mechanics (Das 1941). The geological material used for the tests has been the powder size of the core samples (μm) mixed with small flakes (mm).

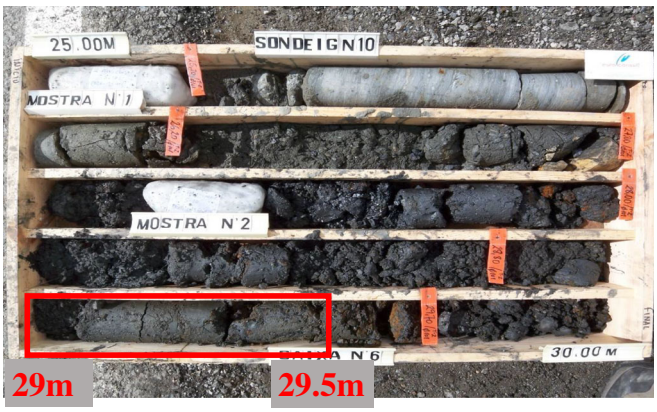

Fig. 3 Core samples preserved of the S10 borehole performed in 2007, including the shear band of the Cal Ponet–Cal Borronet lobe and its center highlighted in a red rectangle. Note that the samples tested in this study are not highlighted in this figure as the tests have been performed on plenty of the core samples from this box

Results

The results of the test performed on the materials of the two boreholes (S9 and S10) will provide information of the "altered" material of the landslide (defined by S10 borehole samples) and the "unaltered" material of the landslide (defined by bedrock shales—S9 borehole). For the material obtained from the S10 borehole, we have considered that each sample studied represents half a meter (in-depth) of the stratigraphic column.

XRPD

Nine samples have been tested in this study. Eight samples are from the S10 borehole, to study the shear band, and one sample is from the S9 borehole, to study the bedrock shales. In total, 6 mineral phases have been found in the nine samples: quartz [SiO_2], muscovite [$K_2Al_4Si_6Al_2O_{20}(OH,F)_4$], chlorite chamosite [$(Mg,Al,Fe)_{12}(Si,Al)_8O_{20}(OH)_{16}$], paragonite [$(K,Na)_2Al_4Si_6Al_2O_{20}(OH,F)_4$], calcite [$CaCO_3$], and plagioclase (albite) [$NaAlSi_3O_8$].

Note that the paragonite found in the XRPD tests and also identified by the SEM-EDS analyses is not pure paragonite mineral, $Na_2Al_4(Si_6Al_2)O_{20}(OH,F)_4$ (Mineral Data Publishing 2001); it is a muscovite rich in sodium (as it is shown in its chemical formula in the paragraph above). However, in this paper, we will refer to it as paragonite (see the "Chemo-mechanical alteration of shales inside the shear band" section for in-depth reasoning).

The percentage (in weight) (wt%) of the identified mineral phases has been calculated by the Rietveld method (Rietveld 1969) and by using the TOPAS V4.2. software.

Figure 4 presents the results of the quantitative analyses (in wt%) of the mineral phases present in nine samples. The sample located at 25.5–26 m depth is mainly composed of calcite (52 wt%), quartz (12 wt%), muscovite (25 wt%), and chlorite chamosite (11 wt%). Its mineral composition is very different compared with the rest of the studied samples. Samples 26.5–27 m and 27–27.5 m are formed by quartz (between 35 and 28 wt%), muscovite (between 55 and 52 wt%), chlorite chamosite (between 16 and 13 wt%), and with minor presence of calcite ($\leq$1 wt%). Five of the analyzed samples present a very similar composition and proportion of the identified minerals, which are 27.5–28 m, 28–28.5 m, 28.5–29 m, 29–29.5 m, and 29.5–30 m. In these samples, a muscovite rich in Na has been identified as a mineral called paragonite. In all the analyzed samples, the presence of quartz varies between 24 and 21 wt%, muscovite between 59 and 53 wt%, paragonite between 22 and 14 wt%, and chlorite chamosite between 6 and 3%. The sample that corresponds to the Silurian shales, which is the bedrock's material, is very rich in muscovite (80 wt%), plagioclase (albite 12 wt%), quartz (8 wt%), and 1 wt% of chlorite chamosite. The latter is the only sample where feldspar (albite) has been detected.

Therefore, the changes in the colors of the core samples seen in Fig. 3 are explained by the mineralogy. Calcite content of sample 25.5–26 m explains the white-ish color, samples from 26.5 to 27.5 with high content in chlorite present a green tone, and samples from 28 to 30 m depth have a high content in muscovite and paragonite which makes the material look darker (black-gray tones also influenced by the organic matter).

SEM-EDS

SEM-EDS analyses have confirmed the mineral composition of the phases found in the samples analyzed by XRPD. In the case of paragonite, EDS analyses reveal the presence of Na in the chemical composition. Moreover, the potassium phyllosilicate present in the studied samples is defined as muscovite due to the amount of K in the mineral composition (Deer et al. 1962). The results of all the studied samples revealed four different textures. Thus, we will present the results of the sample's textures by groups, naming them *textural groups*.

Before we start describing the textural groups observed in the analyzed samples of the S10 borehole, we will first describe the Silurian shales of the bedrock (S9 borehole). The texture of the bedrock's material is considered in this study as the "initial" texture of the shales of the S10 borehole. Therefore, comparing the textures of the bedrock and the shear band can shed light on the possible processes that the material of the shear band has experienced.

The Silurian shales, that constitute the bedrock's material of the study area, are considered in this study as "unaltered" shales. The tested geological material has been obtained from the S9 borehole of the El Forn landslide at 174–175 m depth. This sample presents a highly folded texture and random orientation of the folds and the mica particles but shows a fluid texture of the platy grains of muscovite with face-edge and face-face contacts. Figure 5 shows three SEM-EDS images of this sample at three scales. In Fig. 5a, the minerals are arranged to form very irregular folds that are randomly oriented. The sinuosity of these folds is also very different (as the red lines show in Fig. 5a). Figure 5b presents a large fold of chlorite (white grains) surrounded by multiple randomly oriented smaller folds of muscovite (gray grains). The sinuosity at a smaller scale of the folds can be seen in Fig. 5c, which shows the different orientations and degrees of sinuosity of the folds of the Silurian shales.

The samples analyzed from the S10 borehole represent the shear band and its surroundings, and are described by textural groups by their fabric differences as follows:

- The *first textural group* is defined by sample 27–27.5 m. This material is a black-gray-green shale with several small fractures—filled by quartz (Fig. 6a)—surrounded by phyllosilicates (muscovite, paragonite, and chlorite). Muscovite particles are randomly oriented (Fig. 6b) but showing a fluidal texture of the platy grains of muscovite, with face-edge and face-face contacts. Quartz grains are found inside the subhorizontal fractures with different thickness sizes between bands of phyllosilicates. There is also a presence of accessory minerals, identified by SEM-EDS analyses, such as apatite ($CaPO_4$) and allanite $[Ca,(REE)^{3+}Al_2Fe^{2+}[Si_2O_7][SiO_4]O(OH)]$, among others that are very rich in REE—Ce, La, and Nb. Figure 6c shows an area composed of phyllosilicates. These phyllosilicates (with the presence of quartz) present as fine-grained particles at the boundaries of the quartz veins.
- The *second textural group* is defined by sample 27.5–28 m. The texture of this sample is different from the rest. SEM-EDS images show large fragments of black-gray-green shales (Fig. 6d) and, between them, small particles of quartz and phyllosilicates (muscovite, paragonite, and chlorite) with face-face and face-edge contacts. The texture inside the large clasts is identical to the texture of the first textural group—27–27.5 m sample (Fig. 6e). These large fragments are not matrix-supported as the small particles of quartz and phyllosilicates are not attached (Fig. 6f). Also, this sample has the presence of rutile (TiO_2) (Fig. 6f).
- The *third textural group* is defined by samples 28–28.5 m, 28.5–29 m, and 29.5–30 m. These samples are black-gray shale with small (14 μm) and large (over 75 μm) fractures (filled by quartz), located between layers of phyllosilicates (muscovite, paragonite, and chlorite), and arranged forming folds. Phyllosilicate particles have a certain orientation and direction, following the shape of the folds (Fig. 6g), and their contacts are mainly face-edge, but with some face-face contacts. Quartz grains are located between phyllosilicates following the orientation of the folds (Fig. 6h). Moreover, these samples present accessory minerals such as rutile and hematite (Fe_2O_3). Figure 6i presents a detailed image of muscovite particles and chlorite-muscovite intergrowths.

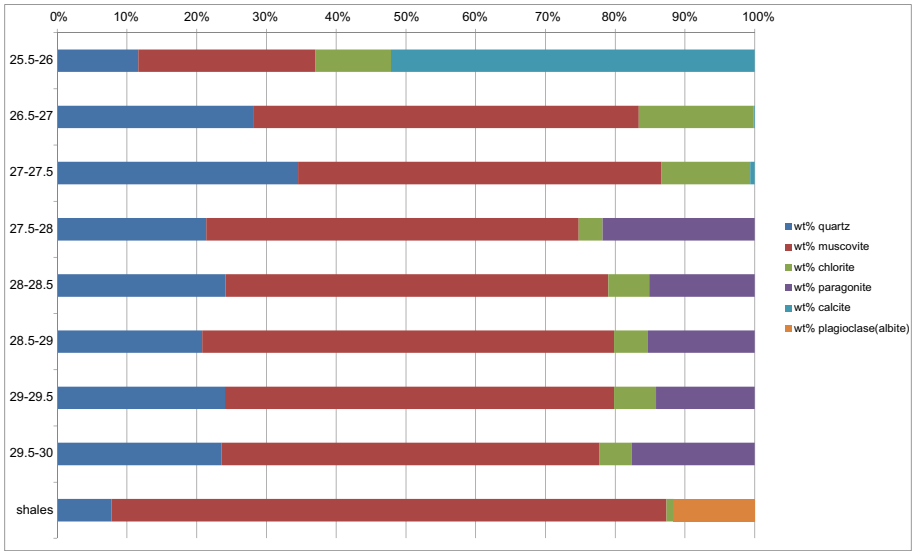

Fig. 4 Proportion in wt% of minerals in each sample studied. wt% is obtained by Rietveld refinement of powder X-ray diffractograms by using the TOPAS V4.2 software

– The *fourth textural group* is defined by sample 29–29.5 m, where the center of the shear band has been found. It is a homogeneous and very dark sample with large and oriented fractures filled by quartz. SEM-EDS images show a well-defined orientation and direction of the phyllosilicates—muscovite, paragonite, and chlorite (Fig. 6j). This sample also presents thick fractures where, at their boundaries, the phyllosilicates are aligned (by their faces) parallel to the fractures (Fig. 6k). Furthermore, contacts between crystals of phyllosilicates are face-face (Fig. 6l).

The sizes of the phyllosilicates, in the analyzed samples, have been obtained by SEM-EDS, and vary between 6 and 50 μm.

MicroCT

Six samples of the S10 borehole have been tested to study the porosity of the material by MicroCT scanning. The results shown in Fig. 7 are for three samples, one of each mechanical group (slightly different from textural groups). We will also show the numerical results (i.e., percentage of porosity) of all samples to see the evolution of the porosity along the shear band.

The *first mechanical group* is defined by samples 27–27.5 m, 27.5–28 m, and 28–28.5 m. These samples present a matrix volume fraction of 0.226, 0.2, and 0.23 and a porosity volume fraction of 0.0029, 0.0027, and 0.0027, respectively. Thus, the samples have a percentage of pores of 1.27%, 1.37%, and 1.15%, respectively. Sample 27.5–28 m (Fig. 7) represents this first mechanical group and presents a defined orientation and direction of small pores and some large fractures.

The *second mechanical group* is defined by samples 28.5–29 m and 29.5–30 m. These two samples have a matrix volume fraction of 0.14 and 0.22, and a porosity volume fraction of 0.00021 and 0.00019, thus with a percentage of pores in the sample of 0.14% and 0.087%, respectively. Sample 29.5–30 m is presented in Fig. 7 and represents this second mechanical group. In Fig. 7, there can be seen very thin and large fractures, with an NW-SE direction (of the image, not the field), across the entire 29.5–30 m sample.

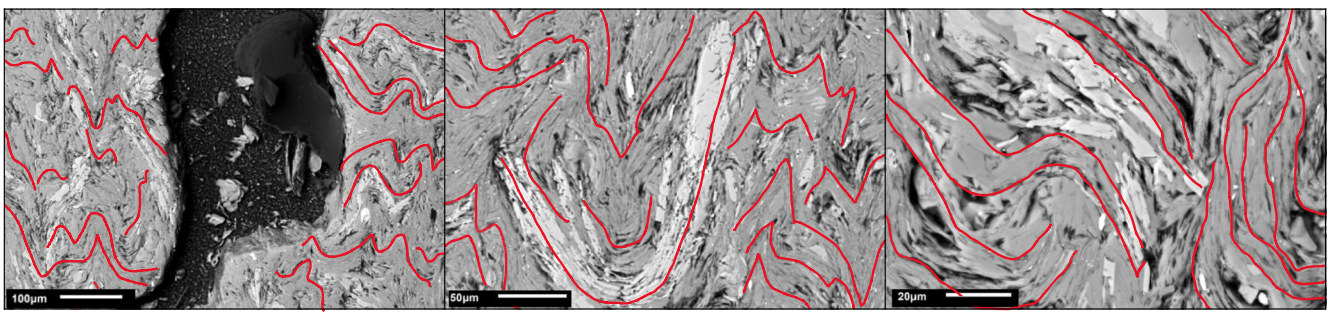

Fig. 5 SEM-EDS images. Backscattered electron (BSE) images of bedrock Silurian shale sample. **a** In this image, phyllosilicates (white particles are chlorite chamosite, and gray particles are muscovite) at both sides of a wide fracture can be seen. **b** This image shows a big fold of chlorite chamosite (white particles) surrounded by smaller and irregular folds of muscovite (gray particles). **c** Irregular and randomly oriented folds formed by phyllosilicates (white is chlorite, and gray is muscovite) with the presence of quartz

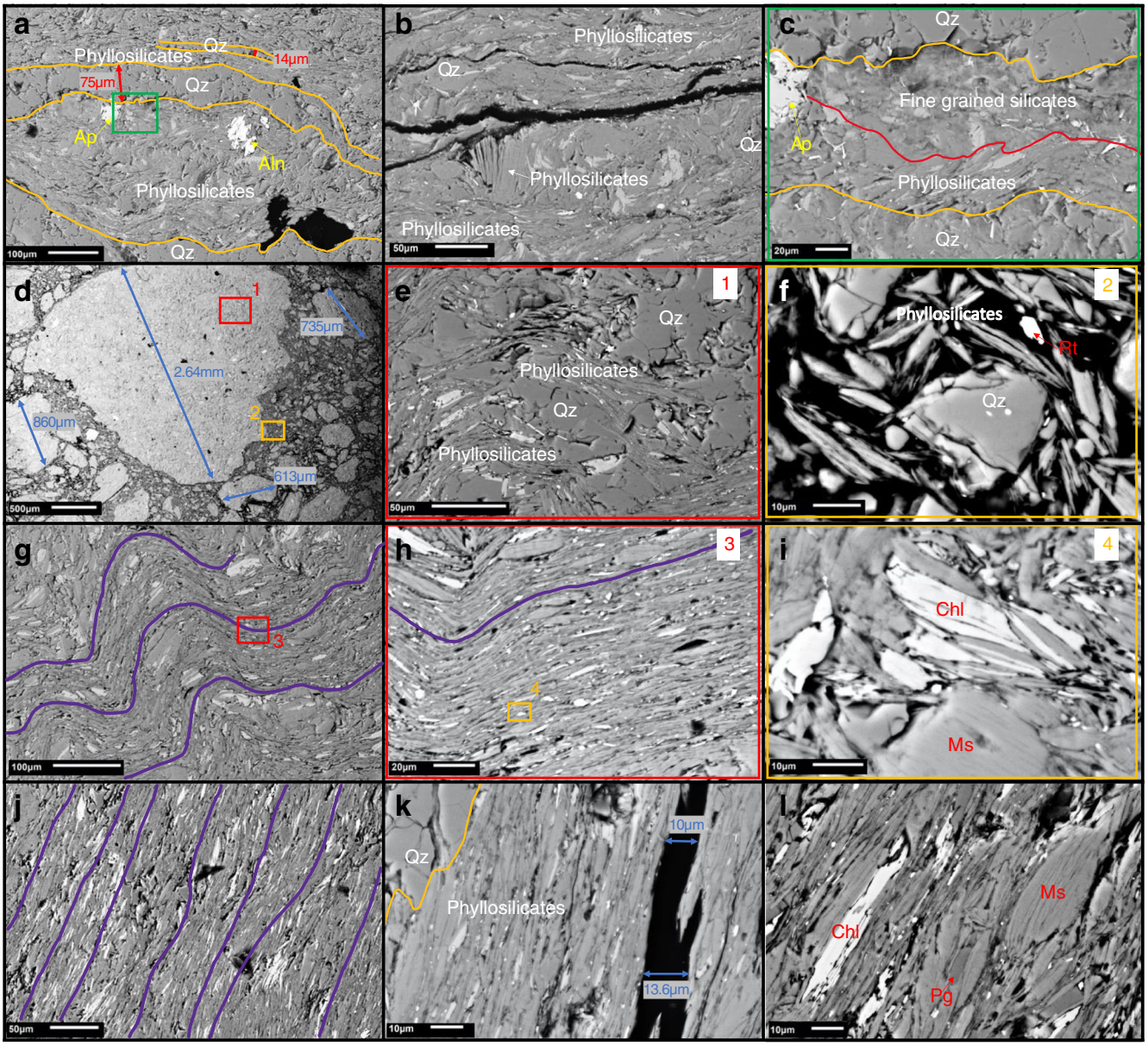

Fig. 6 SEM-EDS images. First textural group. **a** BSE of sample 27–27.5 m. In this image, the main mineralogy is quartz [Qz] and phyllosilicates. The image shows the thickness variability of quartz veins (see yellow lines). There are present accessory minerals of elevating reflectivities such as apatite [Ap] (very light gray color) and allanite [Aln] (vivid white color). **b** BSE of sample 27–27.5 m: phyllosilicates are randomly oriented. **c** BSE of sample 27–27.5 m. Zoom of Fig. 6a (green rectangle). At the top and bottom parts of the image, there are large blocks of quartz (yellow lines) and, in between, fine-grained silicates particles. Second textural group. **d** BSE of sample 27.5–28 m. Fragments of shales of different sizes surrounded by small particles of quartz and phyllosilicates. **e** BSE of sample 27.5–28 m. Zoom of the red rectangle 1 from Fig. 6d. Detail of a fragment of shale where the texture of minerals can be observed. In this case, there are no visible veins of quartz. Quartz grains are randomly oriented and surrounded by phyllosilicate particles oriented forming folds. The orientation of the phyllosilicates is variable, either following a fold or randomly. **f** BSE of sample 27.5–28 m. Zoom of the yellow rectangle 2 from Fig. 6d. Small particles of quartz and phyllosilicates located between large shale fragments. There are large particles (23 μm) of quartz slightly fractured, and small particles of muscovite [Ms] (prismatic shape). There is also a rutile [Rt] mineral (vivid white color). Third textural group. **g** BSE of sample 28.5–29 m. Folds are well defined (purple lines) by oriented phyllosilicates in the direction of the fold. Quartz particles are randomly positioned along the folds. **h** BSE of sample 28.5–29 m. Zoom of red rectangle 3 from Fig. 6g. Orientation detail of phyllosilicates in a syncline (purple line). **i** BSE of sample 28.5–29 m. Zoom of yellow rectangle 4 from Fig. 6g. Detail of quartz, muscovite, chlorite [Chl] particles, and an intergrowth of chlorite-muscovite. Fourth textural group. **j** BSE of sample 29–29.5 m. The clear orientation of phyllosilicates in one direction (parallel to shear movement). **k** BSE of sample 29–29.5 m. A large vein of quartz (yellow line) with phyllosilicates oriented in one direction (see particles interconnected by face-face). There is also a large porous fracture (black) in the middle of the image. Surrounding the fracture, phyllosilicates follow its orientation and direction. **l** BSE of sample 29–29.5 m. Oriented phyllosilicates: muscovite (gray), paragonite [Pg] (dark gray). Note that symbols of minerals are from Whitney and Evans (2010)

Furthermore, this sample presents small pores that are aligned and organized in bands, have the same direction, and look as thin fractures.

The *third mechanical group* is defined by sample 29–29.5 m. This sample presents a matrix volume fraction of 0.14 and a porosity volume fraction of 0.0033, thus with a percentage of pores in the sample of 2.16%. This sample presents, at its center, a large fracture (Fig. 7) with large interconnected pores (where fluid can flow through them). This large fracture has an E-W direction (of the image, not the field). Above and below this fracture, there are thin fractures (some of them located at the bottom of the sample with larger pores) oriented parallel to the shear movement.

Plasticity index

In this section, we present the plasticity index results in relative values (i.e., all results obtained will be divided by the value obtained for the first sample, 27–27.5 m). We present the results in relative values because (1) the values obtained in liquid limit and plastic limit tests usually depend on the user, as each user adds a different amount of water in the samples, and (2) when the borehole was performed, the company obtained a plasticity index value of 8.7 for the sample 27.15–27.30 m and now we obtained a plasticity value of 3.96 for the sample 27–27.5 m. This difference in the value of the plasticity index could also be due to the current dry state of the samples, and its preservation after 12 years (since the borehole was performed). However, as the samples were uniformly exposed to the environment, we assume they degraded proportionally.

The results of the plasticity index reveal the same behavior as the porosity results (the "Mechanical evolution of the shear band" section, Fig. 9). These results show three distinct values that can be identified as three mechanical groups (same mechanical groups as MicroCT). The *first mechanical group* includes samples 27–27.5 m, 27.5–28 m, and 28–28.5 m, with values of relative plasticity index of 1, 0.93, and 0.97, respectively. The *second mechanical group* includes samples 28.5–29 m and 29.5–30 m, with relative plasticity values of 0.67 and 0.62, respectively. The samples of the second mechanical group have lower values of relative plasticity index compared with the values of the first mechanical group (over 30% lower). And, finally, the *third mechanical* group, which is constituted by sample 29–29.5 m, has a value of relative plasticity index of 1.95. Thus, this third mechanical group has a very high value of relative plasticity index compared with the other two groups.

Discussion

Chemo-mechanical alteration of shales inside the shear band

With the XRPD analyses, we have seen a difference in the mineralogy between the black shales of the shear band and the black shales of the bedrock (Fig. 4). The initial composition of the black shales of the shear band can be known by the studied samples of the bedrock (S9 borehole), which are composed of quartz, muscovite, chlorite, and albite. However, the "altered" shales, which are considered in this study as shear band's shales (S10 borehole), are composed of quartz, muscovite, chlorite, and paragonite. The presence of paragonite (muscovite rich in Na) and non-appearance of albite (Na feldspar) indicate that chemical and mechanical processes may have occurred, as previous studies state (Livi et al. 1990; Li et al. 1994; Livi et al. 1997; Árkai et al. 2008). Paragonite has been found in Central and SE Europe and the previous authors, among others, have studied the cause of the rare appearance of this mineral in metamorphic rocks, which generally forms in areas of high pressures and low temperatures (Frey 1978, Frey 1987; Árkai et al. 2008). Specifically, in Silurian to Jurassic shales (same shales as of the present study), the appearance of paragonite has been described as extremely rare (Árkai 1983; Árkai and KovÁcs 1986; Árkai et al. 1995; Árkai et al. 2008).

The paragonite found in this study is related to muscovite (as has been explained in the "XRPD" and "SEM-EDS" sections) and presents an intermediate composition between muscovite ($K_2Al_4Si_6Al_2O_{20}(OH,F)_4$) and paragonite ($Na_2Al_4(Si_6Al_2)O_{20}(OH,F)_4$). The result of this paragonite is an intermediate mineral, which is a muscovite rich in sodium ($(K,Na)_2Al_4Si_6Al_2O_{20}(OH,F)_4$). Usually, paragonite is present as intergrowths inside muscovite (Árkai et al. 2008; Gioretti et al. 2003; Jiang and Peacor 1993).

Different mechanisms can be involved in this chemo-mechanical alteration of black shales. Some studies consider that as albite ($NaAlSi_3O_8$) is a mineral rich in sodium, the hydrothermal alteration can contribute to enrich with Na the fluids that circulate through the rock and trigger the formation of paragonite (Chatterjee 1973; Frey 1969, 1978; Frey 1987; Árkai et al. 2008; Gupta and Fareeduddin 2013). However, considering the percentage of albite in the bedrock's Silurian shales (S9 borehole) and percentage of paragonite in the shear band's shales (from S10 borehole sample, 29–29.5 m depth), we can see that the percentage of these two minerals at each sample is almost the same (Fig. 8). Moreover, it is important to overlay that the paragonite in our samples has been seen by SEM-EDS as an intergrowth between muscovite grains, which could explain the chemical reaction between Na and muscovite (Fig. 6l). Moreover, Gioretti et al. (2003) studied processes that lead to the appearance of an intermediate muscovite rich in sodium as an intergrowth between muscovite minerals. The latter authors described that the result of an altered muscovite rich in sodium is formed by an incomplete reaction of muscovite towards paragonite, ending up with an intermediate mineral phase. Therefore, in our case study, we could consider the possibility of hydrothermal alteration of both, albite and muscovite, as both minerals are in contact with each other, especially when albite grains are fully surrounded by muscovite in the bedrock's shale sample. This could explain a process involving fluids and high pressures that trigger the dissolution of albite and, as albite is in contact with muscovite, creating intergrowths of muscovite-paragonite.

The possible chemo-mechanical mechanisms explained in the previous paragraph could have happened in the study case of the El Forn landslide. However, more information, such as updated thermodynamic data, would be needed to understand the change in the mineralogical composition inside the shear band.

Moreover, the percentage of quartz between the bedrock and the shear band is also very different. In five samples of the shear band, the percentage of quartz varies from 24 to 21 wt%, while in the bedrock's shales, it is 8 wt% (Figs. 4 and 8). This difference in the amount of quartz can be interpreted as the formation of fractures inside the rock (possibly due to shear movement) that facilitate hydrothermal fluid transport and consequent precipitation of quartz inside the fractures. This interpretation can be

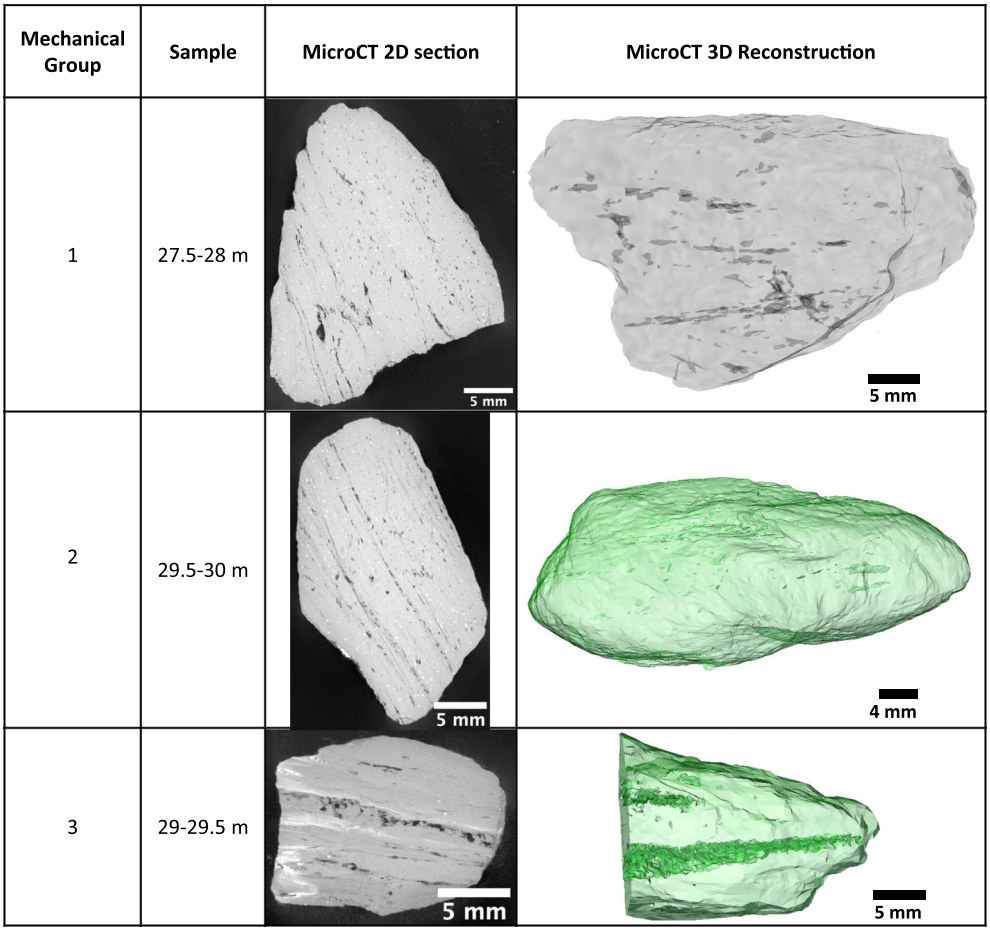

Fig. 7 MicroCT 2D section images, and 3D reconstruction. Each sample shown in this figure represents each mechanical group. Inside 2D section images, black color represents voids/porosity, which in 3D reconstructions is seen as the darker color (dark gray or dark green). In the samples, 27.5–28 m and 29–29.5 m are visually clear in the orientation of pores in the 3D. However, in sample 29.5–30 m, the porosity in the 3D reconstruction is poorly defined as pores are very small (due to low porosity of the sample). Thus, for sample 29.5–30 m, its 2D section image shows visually better orientation of pores (in black). Note that for optimal visualization of the 3D reconstructions, refer to the supplementary videos of the samples

confirmed by the presence of fractures filled by quartz observed in Fig. 6a, c, k.

Mineralogical and textural evolution of the shear band and its comparison with the bedrock's material

With the SEM-EDS analyses, we have been able to characterize and locate the shear band of the El Forn landslide due to the fabric of the S10 core samples. In this section, we present the results and the evolution of mineralogy and fabric of these samples, comparing them with the Silurian shales of the bedrock.

The shear band samples have been characterized by 4 groups, regarding its texture and mineralogy content, called textural groups:

1 The *first textural group* is defined by sample 27–27.5 m. This sample is composed of 35 wt% of quartz, 52 wt% muscovite, 13 wt% of chlorite, and 1 wt% of calcite (Fig. 9). It is the only sample of the S10 that does not have any paragonite, and the only one that has a small content of calcite. Furthermore, this is the sample that has a higher content of quartz (35 wt% compared with 21–24 wt% of the rest of the samples) and chlorite (13 wt% compared with 3–6 wt%) in the shear band area, in which the presence of chlorite (higher amount) makes the sample look greener. Texturally, this sample presents at a small scale (Fig. 6c) a certain orientation, but not a defined direction at a larger scale (Fig. 6b). Although, it can be seen in Fig. 6b that there are partial folds, suggesting that its original texture is the bedrock's shales, there is a noticeable change between this sample and bedrock's shales due to the presence of more grains of quartz. The higher amount of quartz could be explained due to the fractures present in the material. These fractures can also explain that the sample has been fractured due to shear movement and the folds do not have the same continuity as the ones from the initial texture (bedrock's shales).

2 The *second textural group* is defined by sample 27.5–28 m. This sample is composed of 21 wt% of quartz, 53 wt% of muscovite, 3 wt% of chlorite, and 22 wt% of paragonite (Fig. 9). Thus, this sample is the one that has a higher content of paragonite (Fig. 4). The texture of this sample is very different from the rest of

Sample	Thin Section Image	Mineralogy				
		Wt% Qtz	Wt% Mscv	Wt% Chlo	Wt% Parag	Wt% Albite
Silurian Shales		8 %	80 %	1 %	-	12 %
29-29.5 m	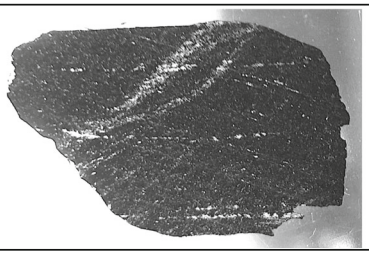	24 %	56 %	6 %	14 %	-

Fig. 8 Images of thin sections and mineralogy (in wt%) of the bedrock's Silurian shale from the S9 borehole and sample 29–29.5 m from the S10 borehole

the samples of the shear band area. This sample presents large angular grains (Fig. 6d) composed by quartz and phyllosilicates (Fig. 6e), and between the large grains are small fragments of phyllosilicates, but not a dense matrix (Fig. 6f), showing a clast support. The texture inside large clasts is the same as the sample of the first textural group and the Silurian shales of the bedrock. Therefore, since the fabric inside the clasts is the same as the first textural group and the bedrock, but the sample has been mechanically altered (showed by the clasts and small fragments), we interpret here that this mechanical alteration is presented as a brittle-viscous deformation of the structure. This mechanical deformation in the sample implies that the shear band deformation starts at this depth, also shown by the vertical deformation of the extensometer in Fig. 1d.

3 The *third textural group* is defined by samples 28–28.5 m, 28.5–29 m, and 29.5–30 m. These samples have the following composition: 24 wt%, 21 wt%, and 24 wt% of quartz; 55 wt%, 59 wt%, and 24 wt% of muscovite; 6 wt%, 5 wt%, and 5 wt% of chlorite; and 15.13 wt%, 15.32 wt%, and 17.5 wt% of paragonite, respectively (Fig. 9). The percentages of the mineralogical composition are very similar in all the three samples. In general, the texture of these samples is very similar as well, where the phyllosilicates have a certain orientation and direction following folds (Fig. 6g and h). The folds present in this textural group are different from the folds of the first and second textural groups, as well as the folds from the bedrock's shales. In this case, the sinuosity of the folds is smoother and the folds are more continuous in the sample. The comparison of the shape of the folds of this third textural group with the ones from the previous textural groups suggests a rearrangement of the phyllosilicates due to higher pressures and shearing movement (Moore and Lockner 2004).

4 The *fourth textural group* is defined by sample 29–29.5 m. This sample is composed of 24 wt% of quartz, 56 wt% of muscovite, 6 wt% of chlorite, and 14 wt% of paragonite (Fig. 9). Thus, this sample could be included inside the third textural group by its mineralogical composition. However, because of its texture, this sample requires to be included in an additional textural group. The texture of this sample is different from the others, as there are no folds (Fig. 6j) as the phyllosilicates are aligned and oriented in one direction (Fig. 6k). The contacts between the phyllosilicates are face-face (Fig. 6l), which is the weakest contact between phyllosilicates (Moore and Lockner 2004). This kind of contact between grains of phyllosilicates and their orientation facilitates friction between grains and the formation of fractures in the same orientation and direction (Fig. 6k). The total orientation of grains along the entire sample identifies it as the area of intense deformation, because of mechanical stresses acting due to friction. The high stresses acting at this depth, due to shear movement, trigger the rearrangement of the grains to a parallel orientation to the shear movement (Moore and Lockner 2004).

Mechanical evolution of the shear band

The mechanical properties of the S10 borehole's samples have been determined by its porosity and index of plasticity. We have characterized these samples by three groups, regarding its porosity and plasticity index, called mechanical groups:

1 The *first mechanical group* is defined by samples 27–27.5 m, 27.5–28 m, and 28–28.5 m. This first group presents a porosity between 1.15 and 1.27% (Fig. 9). Small pores are, generally, located within the entire sample with a defined orientation (parallel to shear direction). However, the pores tend to be at the bottom of the samples (Fig. 7). The porosity in these samples is not connected, as the pores are isolated. Fractures inside the samples follow the same direction as the pores (Fig. 7), which indicates the direction of the shear movement. The values of the plasticity index in these samples are very similar, varying between 0.93 and 1 (Fig. 9). Thus, these three samples—located outside the high mechanical stress area (i.e., shear band)—have the same properties regarding their porosity and plasticity index.

2 The *second mechanical group* is defined by samples 28.5–29 m and 29.5–30 m. These two samples are located right above and

below the area of intense deformation, and they present the lowest porosity values of this study, between 0.087 and 0.14% (Fig. 9). In general, the sizes of the pores that are present in these samples are very small, and not connected, but they are organized in the same orientation (i.e., shear direction), which is the same as the fractures formed in these samples (Fig. 7). The plasticity values in these samples are also very similar, with values between 0.62 and 0.67 (Fig. 9), which are the lowest ones compared with the rest of the studied samples. Thus, in light of these results, it can be considered that right above and below the area of intense deformation there is a strong mechanical behavior that produces a reduction of porosity and plasticity in the samples due to the reorganization of mineralogy because of large deformation and high stresses. With the SEM-EDS analysis, plasticity index, and MicroCT of these two samples, we see that these samples have been under high stress due to the shear movement. Thus, these results lead to assume that they are forming the upper and lower boundaries of the shear band.

3 The *third mechanical group* is defined by sample 29–29.5 m. This sample has been identified as the area of intense deformation of the shear band of the deep-seated landslide. The study of porosity revealed a thick fracture in the entire sample (Fig. 7), which indicates a path of fluid flow. The porosity of this sample is the highest one compared with the rest of the samples studied, with a value of 2.16% (Fig. 9). All pores in this sample are concentrated and connected forming a thick and large fracture (Fig. 7). Furthermore, the plasticity index in this sample is the highest one compared with the rest of the studied samples, with a value of 1.95 (Fig. 9). This high index of plasticity is not related to its mineralogical composition, like the rest of the samples have the same composition and percentage values of minerals (Fig. 9), but to its fabric/texture (Chester and Logan 1987; Collettini et al. 2009; Tchalenko 1968; Maltman 1987; Moore and Lockner 2004). This high plasticity index can be explained by (A) the orientation of phyllosilicates, which is parallel to the shearing direction (Fig. 6k) and (B) the face-to-face contacts between the phyllosilicates (Fig. 6l), which are weaker than edge-edge, corner-face, and corner-edge contacts. Face-face contacts help to increase the plastic behavior of the material, as reflected by the values of the plasticity index calculated in the present study (Labaume et al. 1997). Furthermore, the presence of water in the sample reduces the strength of the material. Moore and Lockner (2004) studied the difference between dry and saturated samples of muscovite and paragonite. The authors found that the friction coefficient of a dry sample of muscovite + paragonite is between 0.5 and 0.6; however, the effect of water decreases this friction coefficient to values between 0.4 and 0.5. They also showed that the presence of fluid creates a film within the phyllosilicate's contacts, reducing its bond and, thus, reducing its friction coefficient (i.e., the strength of the material).>

Fabric and mechanics of a deep-seated landslide

This paper presents the results of the study—at micro-scale—of Cal Ponet–Cal Borronet lobe, which is located inside the large El Forn landslide (Andorra). This lobe is an active deep-seated landslide, as it creeps as a rigid block on top of a heavily deformed shear band. The shear band of this case study is formed of black shales, which are very rich in phyllosilicates (Fig. 4). With the tests performed in the samples of the shear band and the bedrock and its results, it can be seen that there are two kinds of deformation/alteration of the material: chemical and mechanical alterations. Chemical alteration can be seen as the difference of mineralogical composition between shales located in the shear band (considered altered material) and Silurian shales located in bedrock (considered the initial shales), as shown in Fig. 4. The main difference between the altered and the pure Silurian shales is that in the shear band, there is the presence of paragonite (Fig. 8), which is a muscovite rich in Na, and that in the bedrock's shales instead of paragonite, there is albite, which is plagioclase rich in Na. In the previous section (the "Chemo-mechanical alteration of shales inside the shear band" section), we have explained different scenarios that could have led to this chemical process, as the literature cited explains for other case studies. However, the goal of this study is not the study of these chemical processes and further thermodynamic data is needed to understand the chemical reaction produced in these samples. With the data provided in this study and previous studies in the formation of paragonite as intergrowths in muscovite, these indicate that chemo-mechanical processes have occurred. However, it is not probable that the appearance of paragonite has been due to high pressures of the shear movement, as higher pressures than the shearing are needed for the chemical reaction produced at this shallow depth (29 m).

Mechanical alteration due to localized shear movement (active landslide) is explained by the results of the samples' fabric. Results show an evolution of the rearrangement of the minerals, as follows: (1) Outside the shear band, there is no orientation of the mineralogy, as grains are organized creating randomly oriented folds with edge-edge and face-edge contacts. Moreover, the sample of the second textural group can be included here as its fabric inside the clasts is the same as the samples of the first textural group, regardless of the broken structure (thus, showing that mechanical forces have occurred). Hence, we unify both groups for the general picture of the material's behavior along with the shear band of this deep-seated landslide. (2) Closer to the center of the shear band, the fabric of the samples is still folded but the sinuosity and orientation of the folds are more organized and the folds are more continuous than the other samples with folds, and (3) the center of the shear band presents a perfect alignment of the phyllosilicates with face-face contacts, without the presence of folds. This evolution of the texture along with the shear band zone can be observed in Fig. 10 (Carreras et al. 2005). To further describe where the shear band starts and ends, the plasticity index and porosity of the samples have been developed. The values of these two types of test are consistent with the results obtained by the SEM-EDS analysis, where we can describe the same three groups as the ones by SEM-EDS, as (1) the porosity and plastic behavior of the material outside the shear band have a continuous porosity localized in isolated small pores and oriented parallel to flow direction (Fig. 7), and with the same relative value of plasticity index; (2) closer to the center of the shear band, the mechanical results show that both values, of porosity and plasticity index, decrease sharply (Fig. 9). These low values of porosity are due to the rearrangement of minerals forced by shear movement, and the low values in the plasticity index can be explained by the particle's bonds (face-edge) which reduce shear deformation, thus, decreasing its plastic behavior. And (3) the center of the shear band

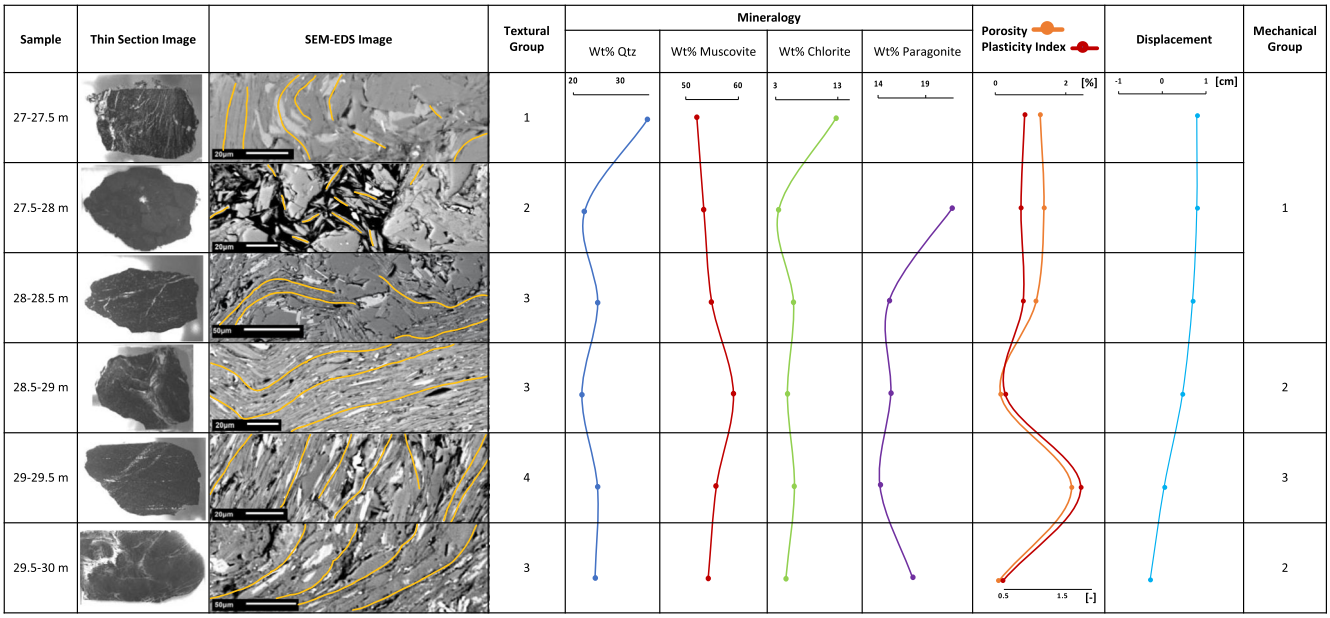

Fig. 9 Combination of all the results performed in the study and its evolution, organized following the stratigraphic column (shallowest at the top to deepest at the bottom). For each sample, the figure shows thin section image, a representative SEM-EDS image with yellow lines following the orientation of the phyllosilicates, mineralogy and its percentage, porosity, relative plasticity index, and displacement from April to June of 2017 (Euroconsult 2017) of the landslide at each corresponding depth

presents a high porosity value, which is localized (mainly) in a thick fracture oriented parallel to the shear movement (Fig. 7). This sample also has a very high value of the plasticity index, compared with the rest of the samples studied (Fig. 9). The plastic

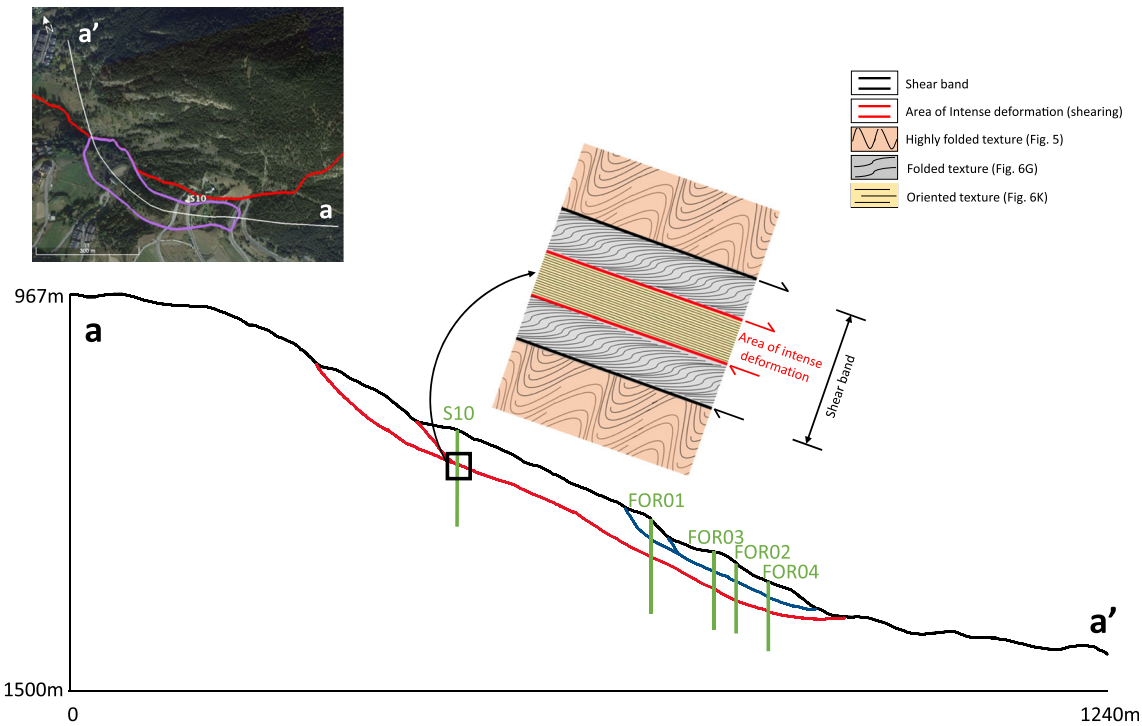

Fig. 10 Profile of Cal Ponet–Cal Borronet lobe with a sketch (taken as a reference from Fig. 9 of Carreras et al. (2005)) of the orientation of mineralogy inside (maximum thickness of each color layer: 0.5 m) and outside the shear band (maximum thickness of layer: 2 m). Green lines represent boreholes (Euroconsult 2008–2018). Note that as the samples tested represent 0.5 m of the stratigraphic column, there is no scale for such a sketch. However, it represents—in dimensionless form—the evolution of orientation of minerals along the stratigraphic column (inside and outside the shear band)

behavior in this area can be explained by texture, which indicates the alignment of phyllosilicates bonded face-face (Fig. 6l), which is the weakest bond between phyllosilicates particles, and this kind of bond increases its plasticity index.

Hence, the difference in mechanical and textural behavior of the material surrounding the area of intense deformation, but at the same time very different from the rest of the samples (outside the shear band), implies that mechanical forces are acting and thus these samples must be included inside the shear band of the El Forn landslide. Therefore, the shear band of the landslide has two types of material: (A) at the edges of the shear band, where the material is still folded and with less porosity and plastic behavior, and (B) at the center of the shear band, where the minerals are perfectly aligned and the porosity and plasticity of the material are very high.

Figure 10 shows the textural evolution of the Silurian shales that are located in the shear band of the El Forn landslide. It has been taken as a reference to the study of Carreras et al. (2005), which explains several scenarios of folded rocks in shear zones. As the sketch in Fig. 10 shows, there is an evolution from outside to inside the shear zone of the El Forn landslide. Outside the shear band of the landslide, the fabric of the shales is the same as the bedrock's shales (no defined orientation and direction of the mineralogy). The folds present in the material outside the shear band show high sinuosity but, as the material is located nearby the shear band, the presence of fractures (mainly filled by quartz) breaks the initial continuous folds (bedrock's shales) ending up with a more chaotic orientation and shorter folds. Inside the shear band of the El Forn landslide, we have seen two types of material with different fabric and mechanical properties: (1) smoother folds (than the initial shales) and very continuous, (2) linear orientation of the mineralogy parallel to the shear movement. In the shear band, the broken and non-oriented folds from the material located outside the shear band start orienting and organizing parallel to the shear movement, due to the shear force and compression. Hence, the folds present inside the shear band are smoother and more continuous. In the center of the shear band (area of high deformation), however, we have seen that the smoother folds have become linear with face-face contacts of the phyllosilicates.

Moreover, it is important to remark that below 30 m depth of the S10 borehole, we do not have samples to present the properties of the material. However, we have considered that as we have symmetry inside the shear band, it should also be symmetric outside the shear band. Leading to assume that the material below 30 m depth is outside the shear band, it has the same properties (textural, mineral, and mechanical) as the material above the shear band (i.e., samples 27–28.5 m depth). Hence, the material below the shear band would have a texture with randomly oriented folds and broken clasts, due to high stresses and deformation in the zone by shearing (Fig. 1d). Therefore, we assume that the evolution of textural and mechanical properties inside and outside the shear band is symmetric (Fig. 10) (Carreras et al. 2005).

Conclusions

This study has correlated the mineralogy content, between mineral phases (by X-ray diffraction), the orientation of the grains (by SEM-EDS), the plasticity index of the material, and the porosity (by MicroCT) in the area of the shear band, to show the effect of the shear movement of a deep-seated landslide.

The tests performed in this study, on the samples of the shear band of the Cal Ponet–Cal Borronet lobe of the El Forn landslide, show that mechanical processes are happening in the material, and are related to shearing. We show an evolution of the fabric of the phyllosilicates from a randomly oriented structure, towards a perfectly aligned fabric at the center of the shear band. Furthermore, we link the effect of the fabric of the material with its mechanical properties, such as porosity and plasticity. The shear movement reorganizes the phyllosilicate grains, which are localized in a thin band and aligned and joined by their weakest contacts.

In conclusion, the authors propose that mechanical mechanisms inside the shear band are caused by the shearing movement, triggering a rearrangement of the phyllosilicates (layered silicates) and a different organization of the layers. These face-to-face contacts between the phyllosilicates (001) facilitate the shear movement, as it is the weakest contact between the phyllosilicates (i.e., decreasing the material's strength). Furthermore, if the material is saturated, as found often inside the shear band of a deep-seated landslide, the friction coefficient of the material in these structures can be significantly decreased, as it is the case of the Cal Ponet–Cal Borronet lobe of the El Forn de Canillo landslide. Thus, this study highlights that there is another mechanism that triggers the sliding and further collapse of a deep-seated landslide, such as the alignment of the phyllosilicates inside the shear band. This, in turn, is showing the importance of a microstructural study of the shear band's material on understanding the behavior of the landslide and the risk of potential failure of the sliding mass.

Acknowledgments

Thin sections were made at the "Servei de Làmina prima" from the Faculty of Earth Sciences at Barcelona University, https://www.ub.edu/portal/web/ciencies-terra/lamina-prima. XRPD (http://www.ccit.ub.edu/ES/tm02.html) and SEM-EDS (http://www.ccit.ub.edu/ES/tb07.html) analyses were made and performed at the Scientific and Technological Centers of the University of Barcelona (CCiTUB). MicroCT tests were carried out at the Duke University Shared Materials Instrumentation Facility (SMIF), a member of the North Carolina Research Triangle Nanotechnology Network (RTNN), which is supported by the National Science Foundation (Grant ECCS-1542015) as part of the National Nanotechnology Coordinated Infrastructure (NNCI). Support by the NSF CMMI-2006150 project is also acknowledged. Liquid and plastic limit tests were carried out at the Soil Mechanics Laboratory at Duke University. The authors acknowledge the help of the laboratory technician Michael Blagg in performing the tests.

References

Altimir J, Copons R, Amigó J, Corominas J, Torrebadella J, Vilaplana JM (2001). Zonificació del 28tructural segons el grau de perillositat d'esllavissades al Principat d'Andorra. Primeres Jornades del CRECIT (IEA), La gestió dels riscos naturals. 119–132

Anderson DL (1980) An earthquake induced heat mechanism to explain the loss of strength of large rock and earth slides. In: Proceedings of the International Conference on Engineering for Protection from Natural Disasters, pp. 569–580. John Wiley, New York

Árkai P (1983) Very low- and low-grade Alpine regional metamorphism of the Paleozoic and Mesozoic formations of the Bükkium, NE-Hungary. Acta Geol Hung 26:83–101

Árkai P, KovÁcs S (1986) Diagenesis and regional metamorphism of the Mesozoic of Aggtelek–RudabÁnya Mountains (Northeast Hungary). Acta Geol Hung 29:349–373

Árkai P, Balogh K, Dunkl I (1995) Timing of low-temperature metamorphism and cooling of the Paleozoic and Mesozoic formations of the Bükkium, innermost western Carpathians, Hungary. Geol Rundsch 84:334–344

Árkai P, Livi KJT, Horváth P (2008) Dioctahedral mixed K-Na-micas and paragonite in diagenetic to low-temperature metamorphic terrains: bulk rock chemical, thermodynamic and textural constraints. Central Eur Geol 61/4:283–314

Barnolas A, Chiron JC (1996). Synthèse Géologique et Géophysique des Pyréenées, Volume 1: Introduction. Géophysique. Cycle Hercynien, 729 pp, BRGM-ITGE, Orléans, France

Bruker (2007) X-ray diffraction software. Diffrac Plus Evaluation Software

Carreras J, Druguet E, Griera A (2005) Shear zone-related folds. J Struct Geol 27:1229–1251

Cecinato F, Zervos A, Veveakis E (2011) A thermo-mechanical model for the catastrophic collapse of large landslides. Int J Numer Anal Methods Geomech 35:1507–1535

Cecinato F, Zervos A (2012) Influence of thermomechanics in the catastrophic collapse of planar landslides. Can Geotech J 49(2):207–225

Chang K, Taboada A, Lin M, Chen R (2005) Analysis of landsliding by earthquake shaking using a block-on-slope thermo-mechanical model: example of Jiufengershan landslide, Central Taiwan. Eng Geol 80:151–163

Chatterjee ND (1973) Low-temperature compatibility relations of the assemblage quartz-paragonite and the thermodynamic status of the phase rectorite. Contrib Mineral Petrol 42:259–271

Chester FM, Logan JM (1987) Composite planar fabric of gouge from the Punchbowl Fault, California. J Struct Geol 9(5/6):621–634

Clariana P (2004) El sinclinori de Tor-Casamanya. Estudi estratigràfic i estructural, Nova cartografia geológica a escala 1:25000. Rev Centre Recerca Cièn Terra, Horitzó 6:3–15

Coelho AA (2000) Whole-profile structure solution from powder diffraction data using simulated annealing. J Appl Crystallogr 33(3 Part 2):899–908. https://doi.org/10.1107/S002188980000248X

Collettini C, Niemeijer A, Viti C, Marone C (2009) Fault zone fabric and fault weakness. Nature 462(7275):907–910. https://doi.org/10.1038/nature08585

Corominas J (1990) Influencia del glaciarismo cuaternario en la estabilidad de laderas del valle del Valira d'Orient (Andorra). I Reunión Nacional de Geomorfología. Teruel. pp. 521–532

Corominas J, Alonso E (1984) Inestabilidad de laderas en el Pirineo catalÁn: tipología y causas. Jornadas Inest. Laderas en el Pirineo. C1-C53. Barcelona

Corominas J, Moya J, Lloret A, Gili JA, Angeli MG, Pasuto A, Silvano S (2000) Measurement of landslide displacements using a wire extensometer. Eng Geol 55:149–166

Corominas J, Iglésias R, Aguasca A, Mallorquí JJ, Fàbregas X, Planas X, Gili JA (2013) Consideraciones sobre el deslizamiento del Forn de Canillo (Principat d'Andorra) a partir de datos de interferometría radar y nuevas observacions sobre el terreno. VIII Simposio Nacional sobre Taludes y Laderas Inestables. Palma de Mallorca, Junio 2013

Corominas J, Iglesias R, Aguasca A, Mallorquí JJ, Fàbregas X, Planas X, Gili JA (2015) Comparing satellite based and ground based radar interferometry and field observations at the Canillo landslide (Pyrenees). Engineering Geology for Society and Territory, Vol. 2

Das BM (1941) Soil mechanics: laboratory manual. 8th ed. ISBN: 978-0-19-984637-5

DeBlasio F, Elverhoi A (2008) A model for frictional melt production beneath large rock avalanches. J Geophys Res 113:F02,014. https://doi.org/10.1029/2007JF000867

Deer WA, Howie RA, Zussman J (1962) An introduction to the rock-forming minerals. Longmans, London, 528pp

Euroconsult SA (2002) Estudi de la zonificació del terreny segons la seva problemàtica geològica. Gran moviment del Forn. Parròquia de Canillo. Govern d'Andorra

Euroconsult SA (2007). Campañas testificación de los sondeos del deslizamiento del Forn de Canillo (Andorra)

Euroconsult SA (2008 to 2018). Auscultacions inclinomètriques, piezomètriques y extensomètriques al moviment de massa del Forn

Euroconsult (2017) Auscultacions inclinomètriques, piezomètriques i extensomètriques al moviment de massa del Forn. Ref. U-1586-A23

Ferri F, Di Toro G, Hirose T, Han R, Noda H, Shimamoto T, Quaresimin M, De Rossi N (2011) Low- to high-velocity frictional properties of the clay-rich gouges from the slipping zone of the 1963 Vaiont slide, northern Italy. J Geophys Res 116:B09208

Frey M (1969) A mixed-layer paragonite/phengite of low-grade metamorphic origin. Contrib Mineral Petrol 14:63–65

Frey M (1978) Progressive low-grade metamorphism of a black shale formation, Central Swiss Alps, with special reference to pyrophyllite and margarite bearing assemblages. J Petrol 19:95–135

Frey M (1987) Very low-grade metamorphism of clastic sedimentary rocks. In: Frey M (ed) Low temperature metamorphism. Blackie, Glasgow, pp 9–58

Gioretti G, Monecke T, Kleeberg R, Herzig PM (2003) Intermediate sodium-potassium mica in hydrothermally altered rocks of the Waterloo deposit, Australia: a combined SEM-EMP-XRD-TEM study. Contrib Mineral Petrol 146:159–173

Goren L, Aharonov E (2007) Long runout landslides: the role of frictional heating and hydraulic diffusivity. Geophys Res Lett 34(L07301):1–7

Goren L, Aharonov E, Anders MH (2010) The long runout of the Heart Mountain landslide: heating, pressurization, and carbonate decomposition. J Geophys Res Solid Earth 115(10B):1–15

Gupta S, Fareeduddin (2013) Occurrence of paragonite in the hydrothermal wall rock alteration zone of G.R.Halli gold deposit, Chitradurga Schist Belt, Western Dharwar Craton, southern India. J Geol Soc India 82:461–473

Hartevelt JJA (1970) Geology of the Upper Segre and Valira valleys, Central Pyrenees Andorra/Spain Leidse. Géol Mediterr 45:167–236

Jaqués I (2014) Revisión del deslizamiento de Canillo, Andorra. Bachelor's Thesis. Departamento de Ingeniería del Terreno, Cartogràfica y Geofísica. Universitat Politècnica de Catalunya, Barcelona

Jaqués I (2015) Análisis geomecánico del deslizamiento del Forn de Canillo (Andorra) mediante el programa de elementos finitos Plaxis. Master's Thesis. Departamento de Ingeniería del Terreno, Cartogràfica y Geofísica. Universitat Politècnica de Catalunya, Barcelona

Jiang W-T, Peacor DR (1993) Formation and modification of metastable intermediate sodium potassium mica, paragonite and muscovite in hydrothermally altered metabasites from northern Wales. Am Mineral 78:782–793

Kilburn RJC, Petley DM (2003) Forecasting giant, catastrophic slope collapse: lessons from Vajont, Northern Italy. Geomorphology 54:21–32

Labaume P, Maltman AJ, Bolton A, Tessier D, Ogawa Y, Takizawa S (1997). Scaly fabrics in sheared clays from the décollement zone of the Barbados accretionary prism. Proceedings of the Ocean Drilling Program, Scientific Results, Vol. 156

Lachenbruch AH (1980) Frictional heating, fluid pressure and the resistance to fault motion. J Geophys Res 85:6097–6112

Li G, Peacor DR, Merriman RJ, Roberts B (1994) The diagenetic to low-grade metamorphic evolution of matrix white micas in the system muscovite-paragonite in a mudrock from Central Wales, United Kingdom. Clay Clay Miner 42:369–381

Livi KJT, Veblen DR, Ferry JM (1990). Segregation of K- and Na-rich micas in low-grade metamorphosed shale from the Liassic black shale, Switzerland. IGCP Project No. 294: Very low-grade metamorphism. Conference on Phyllosilicates as Indicators of Very Low Grade Metamorphism and Diagenesis. Programme and Abstracts. Manchester, July 1990

Livi KJT, Veblen DR, Ferry JM, Frey M (1997) Evolution of 2:1 layered silicates in low-grade metamorphosed Liassic shales of Central Switzerland. J Metamorph Geol 15:323–344

Maltman AJ (1987). Shear zones in argillaceous sediments–an experimental study. Geological Society, London, Special Publications, 29 (1):77

Mase CW, Smith L (1984) Pore-fluid pressures and frictional heating on a fault surface. PAGEOPH 122(2–4):583–607. https://doi.org/10.1007/BF00874618

Mineral Data Publishing (2001). Paragonite. Version 1.2

Moore DE, Lockner DA (2004) Crystallographic controls on the frictional behavior of dry and water-saturated sheet structure minerals. J Geophysical Res 109:B03401. https://doi.org/10.1029/2003JB002582

Regenauer-Lieb K, Yuen D, Fusseis F (2009) Landslides, ice quakes, earthquakes: a thermodynamic approach to surface instabilities. Pure Appl Geophys 166(10–11):1885–1908

Rietveld HM (1969) A profile refinement method for nuclear and magnetic structures. J Appl Crystallogr 2(2):65–71. https://doi.org/10.1107/S0021889869006558

Rice J (2006) Heating and weakening of faults during earthquake slip. J Geophys Res 111:B05311. https://doi.org/10.1029/200JB004006

Planas X, Corominas J, Vilaplana JM, Altimir J, Torrebadella J, Amigó J (2011). Noves aportacions al coneixement del gran moviment del Forn de Canillo, Principat d'Andorra. Resúmenes XIII Reunión Nacional de Cuaternario, Andorra la Vella. 5pp. 163-167

Santacana N (1994). Estudi dels grans esllavissaments d'Andorra: Els casos del Forn i del vessant d'Encampadana. En Tesis de Licenciatura. Departamento de Geología, Dinàmica, Geofísica i Paleontología de la Facultad de Geología de la UB. pp. 1–169

Segui C, Rattez H, Veveakis E (2020). On the stability of deep-seated landslides. the cases of Vaiont (Italy) and Shuping (Three Gorges Dam, China), J Geophys Res ES e2019JF005203, doi: https://doi.org/10.1029/2019JF005203

Soutadé G (1988). Le Glissement d'el Forn. II Simposio sobre Taludes y Laderas Inestables. Andorra la Vella, 9-11 de Marzo de 1988. pp.1-15

Tchalenko JS (1968) The evolution of kink-bands and the development of compression textures in sheared clays. Tectonophysics 6(2):159–174

TJP (2015) Avizo Guide. Avizo training materials, BRC-Imaging Facility
Torrebadella J, Villaró I, Altimir J, Amigó J, Vilaplana JM, Corominas J, Planas X (2009) El deslizamiento del Forn de Canillo en Andorra. Un ejemplo de gestión del riesgo geológico en zonas habitadas en grandes deslizamientos (in Spanish). In: Proceed. VII Simposio Nacional sobre Taludes y Laderas Inestables, held in Barcelona, Oct 2009. Ed. CIMNE, UPC, pp 403–414
Vardoulakis I (2000) Catastrophic landslides due to frictional heating of the failure plane. Mech Cohesive Frict Mater 5:443–467
Vardoulakis I (2002) Dynamic thermo-poro-mechanical analysis of catastrophic landslides. Géotechnique 52:157–171
Veveakis E, Vardoulakis I, Di Toro T (2007) Thermoporomechanics of creeping landslides: the 1963 Vaiont slide, northern Italy. J Geophys Res 112:F03026. https://doi.org/10.1029/2006JF000702
Voight B, Faust C (1982) Frictional heat and strength loss in some rapid landslides. Géotechnique 32:43–54
Whitney DL, Evans BW (2010) Abbreviations for names on rock-forming minerals. Am Mineral 95:185–187
Zwart HJ (1979). The geology of the Central Pyrenees. Leidse geologische mededelignen, ISSN 0075-8639

Electronic supplementary material The online version of this article (https://doi.org/10.1007/s10346-020-01492-6) contains supplementary material, which is available to authorized users.

C. Seguí (✉) · **M. Veveakis**
Civil and Environmental Engineering Department,
Duke University,
Durham, NC, USA
Email: carolina.segui@duke.edu

E. Tauler
Departament de Mineralogia, Petrologia i Geologia Aplicada,
Universitat de Barcelona,
Barcelona, Spain

X. Planas
Ministeri d'Ordenament Territorial,
Govern d'Andorra,
Andorra la Vella, Andorra

J. Moya
Departament d'Enginyeria Civil i Ambiental,
Universitat Politècnica de Catalunya,
Barcelona, Spain